Microchemical Journal 218 (2025) 115528

Contents lists available at ScienceDirect

Microchemical Journal

journal homepage: www.elsevier.com/locate/microc

Rapid visual detection of aspartame based on SWCNTs-TiO_2 nanomaterial-modified bioenzyme sensor

Xin Li [a], Lei Li [a,b], Ping Jiang [a,b,*]

[a] Center for Global Health, School of Public Health, Nanjing Medical University, 101 Longmian Avenue, Nanjing, Jiangsu 211166, PR China
[b] The Key Lab of Modern Toxicology of Ministry of Education, School of Public Health, Nanjing Medical University, 101 Longmian Avenue, Nanjing, Jiangsu 211166, PR China

ARTICLE INFO

Keywords:
Aspartame
Electrochemical biosensor
SWCNTs-TiO_2 nanocomposite
Dual-enzyme system
Visual detection

ABSTRACT

Given the potential health hazards of aspartame, developing simple, rapid, and sensitive detection technologies remains challenging. Herein, we propose a nanomaterial-modified dual-enzyme biosensor for the qualitative and quantitative detection of aspartame. The biosensor uses a Screen-printed Carbon Electrode (SPCE) modified with a single-walled carbon nanotube-titanium dioxide nanocomposite (SWCNTs-TiO_2) and integrates a dual-enzyme system (Alcohol Oxidase, AOX; Carboxylesterase, CaE). Bovine Serum Albumin (BSA), AOX, and CaE were immobilized on the SWCNTs-TiO_2/SPCE using Glutaraldehyde (GA) as a cross-linking agent. The dual-enzyme system specifically decomposes aspartame to generate Hydrogen Peroxide (H_2O_2), and the electrode system accelerates this reaction. The produced H_2O_2 further reacts with 3,3′,5,5′-tetramethylbenzidine (TMB) in a custom electrolyte to form a distinct visible blue compound for visual analysis. Notably, SWCNTs enhance the sensor's electrical conductivity. SWCNT-TiO_2's high specific surface area and loose porous network provide abundant active sites for enzyme immobilization and substrate adsorption. TiO_2 nanomaterials exhibit a strong adsorption capacity, enabling the rapid enrichment of target biomolecules. The dual-enzyme-modified electrode surface further facilitates the specific capture of aspartame. Under optimal conditions, the biosensor achieves a limit of detection (LOD) of 0.232 μg/mL in colorimetric mode and 0.131 μg/mL in electrochemical mode. Satisfactory results were obtained in the analysis of real food samples, demonstrating promising potential for the qualitative and quantitative detection of aspartame in food products.

1. Introduction

Since Food and Drug Administration (FDA) approval in 1981, the safety of aspartame remains debated, with conflicting findings from epidemiological and experimental studies [1]. Mounting research associates aspartame with health risks [1]. The International Agency for Research on Cancer (IARC) classifies it as "possibly carcinogenic to humans," citing hepatocarcinogenesis evidence in human and animal studies [2,3]. Aspartame intake correlates with elevated cardiovascular disease risk, and a meta-analysis corroborates its association with hypertension, especially in middle-aged populations [4,5]. Longitudinal studies link aspartame intake to type 2 diabetes, with cohort data showing 15 % higher risk in habitual users [6,7]. Aspartame exposure is associated with increased all-cause mortality risk and neurological sequelae, with preclinical evidence from meta-analyses confirming its link to learning deficits, mood dysregulation, and augmented oxidative stress, particularly in preclinical models [8]. Moreover, potential perturbations in renal function—as evidenced by altered metabolite excretion in renal clearance studies—and their putative role in weight gain and obesity-related pathophysiology merit attention [7,9]. Regulatory bodies like the FDA consider aspartame safe within thresholds, and they set a 60 mg/kg body weight daily intake limit [10,11]. Recent research contests this, highlighting that habitual aspartame intake—even at levels below the Acceptable Daily Intake (ADI)—may confer health risks, particularly in pediatric cohorts [12].

Aspartame is widely used in the food industry, and safety controversies surrounding it persist [13]. Therefore, accurately detecting aspartame in food products is crucial. Existing analytical methods for aspartame can quantify the target analyte, but they have notable limitations. These include complex sample preparation, high instrument costs, and long detection cycle [14–16], which make it hard to meet the demand for on-site rapid detection. Large-scale instrumental techniques

* Corresponding author at: Center for Global Health, School of Public Health, Nanjing Medical University, 101 Longmian Avenue, Nanjing 211166, PR China.
E-mail address: jiangping@njmu.edu.cn (P. Jiang).

https://doi.org/10.1016/j.microc.2025.115528
Received 10 August 2025; Received in revised form 7 September 2025; Accepted 25 September 2025
Available online 30 September 2025

are among these traditional methods, including High-performance Liquid Chromatography (HPLC), Gas Chromatography (GC), Gas Chromatography-tandem Mass Spectrometry (GC–MS/MS), and Liquid Chromatography-tandem Mass Spectrometry (LC-MS/MS) [17,18]. These techniques offer high sensitivity and accuracy, but they rely on expensive equipment, professional operation skills, and tedious pretreatment procedures [19]. This limits their application scenarios. Vibrational spectroscopy techniques are another type of traditional method, such as Fourier Transform Infrared Spectroscopy (FTIR) and Raman Spectroscopy [18,20]. But they show weak anti-interference ability and a narrow detection range [13,21,22]. This further highlights the limitations of traditional methods. It also makes the development of more robust, highly selective detection technologies urgent.

In contrast, electrochemical sensors have distinct advantages, including simple operation, high sensitivity, and low detection cost. They can make up for the pain points of traditional methods and enable efficient detection of aspartame [23]. Electrochemical biosensors incorporating biological recognition elements (e.g., enzymes) provide analytical advantages [4,24,25]. Such biosensors integrate rapid response, cost-effectiveness, portability—hallmarks of on-site applications—and high specificity derived from biorecognition [26–28]. Electrochemical analysis excels in trace detection with ultra-high sensitivity (down to nano- to pico-molar levels) [29]. However, it suffers from poor selectivity, as its signals are easily interfered with by coexisting electroactive species. Additionally, it demands sophisticated instrumentation and specialized operational skills, limiting its accessibility [30]. Colorimetric analysis, conversely, is ideal for on-site rapid screening. It enables straightforward visual readout via color changes, featuring simplicity and low cost [31]. Nevertheless, it is constrained by relatively low sensitivity (typically at the micro-molar level) and unstable quantitative accuracy, which is significantly affected by environmental factors such as temperature, pH, and reaction time [32,33]. To overcome these inherent limitations of individual methods, the electrochemical-colorimetric coupling strategy has emerged. This approach constructs a dual-response system integrating electrochemical and colorimetric signals. It not only retains the high sensitivity of electrochemistry and the high selectivity plus convenience of colorimetry, but also enhances sensitivity further through electrocatalysis-mediated signal amplification. Importantly, only the target analyte can trigger both signal responses simultaneously, greatly improving detection accuracy and anti-interference capability. This synergistic method thus effectively meets the requirements of both precise laboratory analysis and rapid on-site detection.

SWCNTs (nanoscale diameter) combine low specific gravity, ultra-high aspect ratio, high thermal/electrical conductivity, and high elastic modulus, being the fibrous material with the best known mechanical properties [23]. In electroanalytical chemistry, SWCNTs efficiently catalyze electrochemical reactions of biomolecules/inorganic compounds. Compared with standard carbon electrodes, they accelerate electron transfer, reduce overpotential, shorten response time, and boost electroactive substrate reaction rates [24]. In biosensing, TiO_2 nanomaterials have good biocompatibility and strong adsorption, with modifiable surfaces for specific capture. In electrochemical sensors, their redox activity enhances target signals, and high chemical stability ensures reliability in acidic/alkaline electrolytes [34]. TiO_2 is also a widely used photocatalyst with high activity, low cost/toxicity, large specific surface area, and stabilizes enzyme conformation via surface -OH hydrogen bonds [35]. SWCNT-TiO_2 composites exhibit significant synergies: SWCNTs act as “electron bridges” to transfer TiO_2’s electrons, and their combined large specific surface area/TiO_2’s adsorption forms a “dual enrichment effect” [36]. For aspartame detection, SWCNTs accelerate electron transfer, and TiO_2 selectively adsorbs/catalyzes aspartame oxidation. SWCNTs’ size sieving inhibits protein adsorption. TiO_2 modifies SWCNTs’ hydrophobicity. Their synergy significantly enhances the aspartame oxidation peak current, outperforming single-material sensors [37].

In this work, we present a novel electrochemical biosensor. Immobilizing Alcohol Oxidase (AOX), Carboxylesterase (CaE) on SWCNTs-TiO_2 nanocomposite-modified screen-printed carbon electrodes. Aspartame is decomposed into Methanol and L-aspartyl-L-phenylalanine (L-Asp-L-Phe) under the catalysis of Carboxylesterase (CaE). Subsequently, the generated Methanol is further decomposed into Hydrogen Peroxide (H_2O_2) and Formaldehyde under the action of Alcohol Oxidase (AOX). The produced H_2O_2 reacts with 3,3′,5,5′-tetramethylbenzidine (TMB) to turn it blue, enabling visual detection. Notably, we did not use the colorimetric method and the electrochemical method independently. Instead, we integrated these two methods. The fabricated sensor was connected to a portable electrochemical workstation, integrating electrochemical detection and the colorimetric process. This design aimed to construct an on-site visual detection platform that can operate independently of laboratories, require no professional operation, and realize qualitative and quantitative detection of aspartame in food [29,32].

2. Experiment

Detailed information regarding materials, reagents, and instruments is presented in the Supplementary Information.

2.1. Preparation of SWCNTs-TiO_2 nanocomposites

SWCNTs (30.0 mg) and TiO_2 (30.0 mg) were dispersed in 100 mL of deionized water within a 500 mL round-bottom flask. The mixture was sonicated for 35 min using a 400 W bath-type sonicator to achieve homogeneous dispersion. This was then transferred to a 70 °C oil bath and subjected to magnetic stirring for 6 h to facilitate chemical interactions. After stirring, the solution was sonicated again for 35 min to improve the uniformity of the composite. The supernatant was then decanted, and the resulting SWCNTs-TiO_2 dispersion (0.3 mg/mL) was stored at 4 °C for subsequent experiments.

2.2. Fabrication of SWCNTs-TiO_2/SPCE sensor

The SWCNTs-TiO_2/SPCE sensor was prepared via the drop-casting method, and before modification, the SPCE surface was pretreated to enhance film adhesion and electrochemical performance: firstly, the SPCE was immersed in a 1 mol/L NaOH solution (sufficient to cover the entire working area of the electrode) and sonicated for 5 min, after which the electrode surface was thoroughly rinsed with ultrapure water to remove residual NaOH and dried with Nitrogen (N_2) gas. Subsequently, the SPCE was immersed in a 5 mol/L HCl solution (also sufficient to cover the entire working area) and sonicated for another 5 min, followed by thorough rinsing with ultrapure water to eliminate residual HCl, rinsing of the electrode surface with absolute ethanol 2–3 times (2–3 mL of absolute ethanol dropped each time using a dropper) to remove partial fat-soluble or hydrophobic impurities, and gentle drying with high-purity N_2 until completely dry. After pretreatment, 6 μL of the pre-prepared SWCNTs-TiO_2 suspension (0.3 mg/mL) was carefully dropped onto the working area of the pretreated SPCE, and the electrode was dried under ambient conditions (25 °C, relative humidity 40–50 %) for 2 h to ensure complete solvent evaporation and the formation of a uniform nanocomposite film. Finally, the pretreated and modified electrode was immersed in 10–20 mL of Phosphate-buffered Saline (PBS) with a pH of 7.0–7.4 and a concentration of 0.01–0.1 mol/L. An electrochemical workstation was connected, and cyclic voltammetry scans were performed until the curve stabilized, ensuring the electrode reached a stable electrochemical performance state.

2.3. Preparation of SWCNTs-TiO_2/SPCE dual-enzyme sensor

Firstly, Alcohol Oxidase (AOX, 7.7 IU) and Carboxylesterase (CaE, 18.7 IU) were dissolved in 20 μL of phosphate-buffered saline (PBS, 0.1 M, pH 7.4). Then, 5 μL of 0.6 % (w/v) Bovine Serum Albumin (BSA) and

5 μL of 1.5 % (w/v) Glutaraldehyde (GA) were added. After vortexing for 30 s, 4 μL of the mixture was drop-cast onto the SWCNTs-TiO_2-modified working electrode. Then the electrode dried in a desiccator at 25 ± 1 °C for 1 h to promote covalent crosslinking. After fabrication, the sensors were stored at −20 °C in airtight containers with silica gel. Before use, the electrodes were rinsed with PBS to remove any unbound reagents.

2.4. Experimental design for electrochemical-colorimetric combined detection of aspartame

Carboxylesterase (CaE) and Alcohol Oxidase (AOX) immobilized on the sensor surface synergistically catalyze the decomposition of aspartame. The generated Hydrogen Peroxide (H_2O_2) undergoes a colorimetric reaction with 3,3′,5,5′-tetramethylbenzidine (TMB) to form a blue product, enabling rapid preliminary screening and quantitative detection. Current catalysis accelerates the reaction. Meanwhile, H_2O_2 undergoes redox reactions on the surface of the SWCNTs-TiO_2 composite electrode, generating detectable electrochemical signals for accurate quantification. The mutual verification of these two signals improves the reliability of detection. Aspartame standard solutions with concentrations of 0.01, 0.02, 0.03, 0.04, 0.05, 0.06, 0.07, 0.08, 0.09, and 0.1 mg/mL were prepared using PBS. The dual-enzyme electrode modified with nanocomposites was connected to the electrode system, and the standard solutions with different concentrations were detected separately. Linear Sweep Voltammetry (LSV) was employed at a scan rate of 100 mV/s to record current density-potential curves, and an electrochemical standard curve was plotted by taking the oxidation peak current as the ordinate and aspartame concentration as the abscissa. For the generated blue signal, the absorbance at 652 nm (the characteristic absorption peak of the oxidized TMB product) was measured, and a colorimetric standard curve was constructed using absorbance values against aspartame concentrations. Simultaneously, the color changes observed by the naked eye were recorded to establish the corresponding relationship between color and concentration.

3. Results and discussion

3.1. Design strategy of a dual-enzyme biosensor based on nanomaterial modification of SWCNTs-TiO_2/SPCE

The design process of the SWCNTs-TiO_2/SPCE dual-enzyme sensor is illustrated in Fig. 1. Notably, Carboxylesterase (CaE) and Alcohol Oxidase (AOX) were covalently immobilized on the surface of SWCNTs-TiO_2/SPCE. This immobilization was achieved via cross-linking with Bovine Serum Albumin (BSA) and Glutaraldehyde (GA), providing a stable and effective means of attaching the enzymes to the electrode surface. Once immobilization was complete, a dual-enzyme biosensor modified with SWCNTs-TiO_2 nanomaterials was successfully fabricated. The developed sensor enables qualitative and quantitative detection of target samples. Alcohol Oxidase (AOX) and Carboxylesterase (CaE) decompose the aspartame solution to produce Hydrogen Peroxide (H_2O_2). H_2O_2 reacts to generate active hydroxyl (-OH) groups under the catalysis of an electric current, which then reacts with TMB in the solution to show a blue color, enabling visual detection. Qualitative analysis is achieved by observing the solution's color change, while quantitative detection is realized by monitoring variations in the absorbance of the colorimetric signal.

3.2. Morphology and performance characterization of SWCNTs-TiO_2 materials

In this study, Scanning Electron Microscopy (SEM) was utilized to accurately analyze the particle size and morphology of the SWCNTs (Fig. 2A), TiO_2 (Fig. 2B), and synthesized SWCNTs-TiO_2 composite materials (Figs. 2C, D, E, and F). The above results show that the SWCNTs alone exhibited a loosely porous network structure (Fig. 2A). However , a significant morphological change was observed after TiO_2 modification, as shown in Figs. 2C and D; spherical TiO_2 nanoparticles were found dispersed across the mesh-like structure of SWCNTs. The SEM images in Fig. 2E and F show numerous smooth, spherical TiO_2 particles attached to the mesh-like gap in the SWCNTs. The distinct, well-dispersed lattice structure of these particles indicates successful deposition. Furthermore, by comparing the SEM image of pristine SWCNTs without TiO_2 modification (Fig. 2A) and pure TiO_2 (Fig. 2B) with that of SWCNTs-TiO_2, it was verified that the original folded

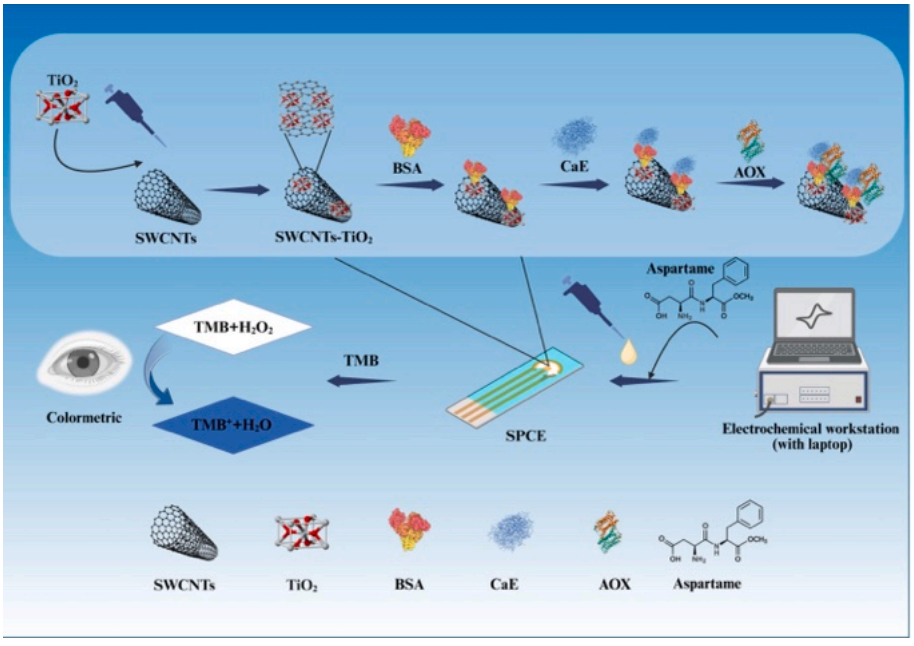

Fig. 1. Flowchart of the preparation process.

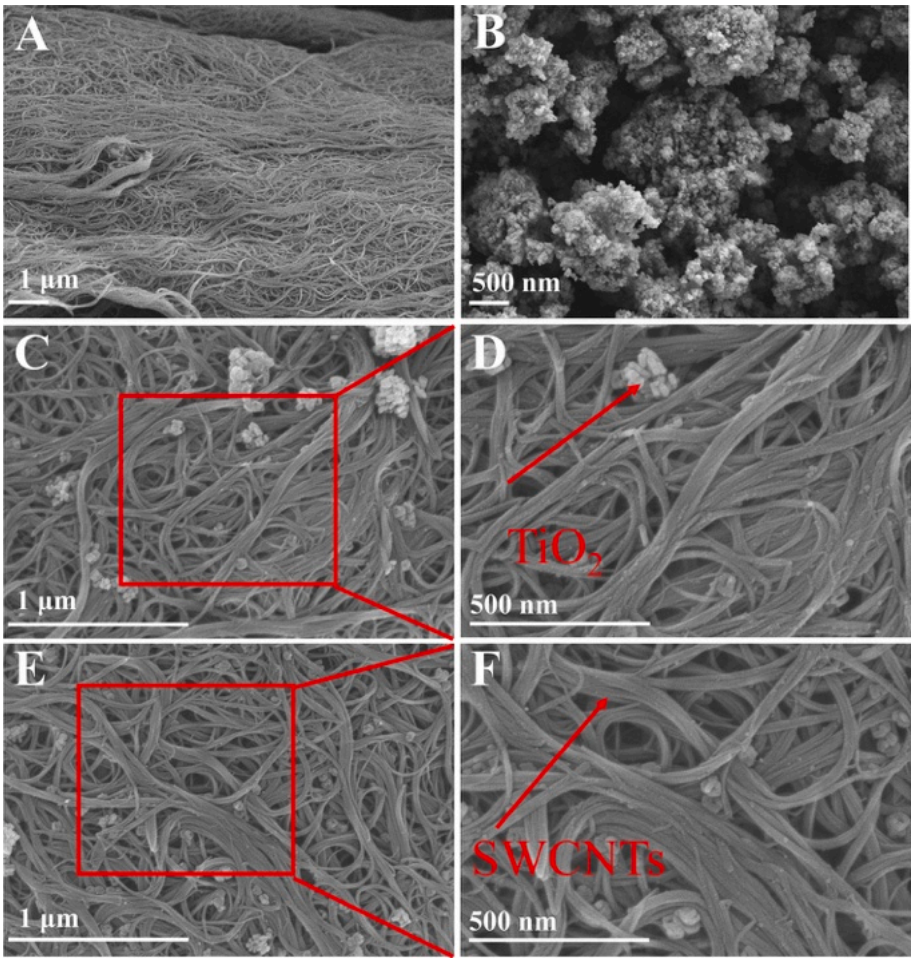

Fig. 2. SEM images of SWCNTs, TiO_2, and SWCNTs-TiO_2 with different magnifications. (A)SEM image of SWCNTs;(B)SEM image of TiO_2;(C, D, E, F)SEM images of SWCNTs-TiO_2.

structure of SWCNTs remained intact throughout the modification process—indicating that the synthesis strategy did not compromise the structural integrity of SWCNTs.

Before the ζ potential testing, the materials were dispersed in ultrapure water maintained at a temperature of 25 °C to ensure a homogeneous and stable suspension. The ζ-potential test results further confirm the successful preparation of the single-walled carbon nanotube-titanium dioxide (SWCNTs-TiO_2) composite (as shown in Table 1). The ζ-potential of pure SWCNTs is −12.6 mV, while that of pure TiO_2 nanoparticles is −21.7 mV. Notably, the ζ-potential of the prepared SWCNTs-TiO_2 composite is −15.2 mV, which lies between the values of the two original components but is not equal to their mass-weighted average. This intermediate ζ-potential can be reasonably explained by the interfacial interaction between SWCNTs and TiO_2. Pure TiO_2 generates a large number of negative charges due to the dissociation of surface hydroxyl groups ($TiO_2 + H_2O \rightleftharpoons Ti\text{-}O^- + H_3O^+$), resulting in a ζ-potential of −21.7 mV. In contrast, SWCNTs have fewer surface defect functional groups (e.g., -COOH) and weak adsorption of anions in the solution, leading to a less negative ζ-potential of −12.6 mV. During the formation of the composite, TiO_2 nanoparticles are anchored on the surface of SWCNTs through non-covalent interactions or partial charge transfer. This interfacial binding regulates the surface charge distribution of the composite: the strong negative charge of TiO_2 is partially "buffered" by the relatively weaker negative charge of SWCNTs, and the surface charge of SWCNTs is in turn affected by the attached TiO_2 particles. Eventually, the composite exhibits a ζ-potential (−15.2 mV) between the two components, reflecting the synergistic effect between the two phases. Importantly, this single intermediate ζ-potential value rules out the possibility of simple physical mixing—physical mixing would exhibit two distinct peaks or a value close to one of the components. This indicates that a homogeneous composite structure is formed in the system, and SWCNTs and TiO_2 achieve tight binding, thereby confirming the successful composite of the two phases.

Table 1
Measurement of ζ potential of TiO_2, SWCNTs and SWCNTs-TiO_2.

Materials	ζ potential (mV)
TiO_2	−21.7
SWCNTs	−12.6
SWCNTs-TiO_2	−15.2

To better confirm the successful synthesis of the composites, X-ray Photoelectron Spectroscopy (XPS) was employed to analyze the elemental properties of the SWCNTs-TiO_2 composites. The presence of distinct peaks corresponding to C1s (Fig. 3A), O1s (Fig. 3B), and Ti2p (Fig. 3C) in the spectra provided direct evidence of the successful fixation of TiO_2 onto SWCNTs-TiO_2. Specifically, the C1s XPS spectrum of SWCNTs post-TiO_2 adsorption deconvoluted into three peaks at binding energies of 290.01 eV (O-C=O), 285.97 eV (C-O-C), and 284.50 eV (C—C), as depicted in Fig. 3A. The O1s XPS spectrum could be resolved into two peaks at 532.64 eV (C=O) and 530.56 eV (C—O), while the Ti2p XPS spectrum exhibited two peaks at 465.09 eV (Ti2p1/2) and 459.38 eV (Ti2p2/3) [34,38–40]. Fig. 3D further corroborated the successful synthesis of the composite material, with the characteristic

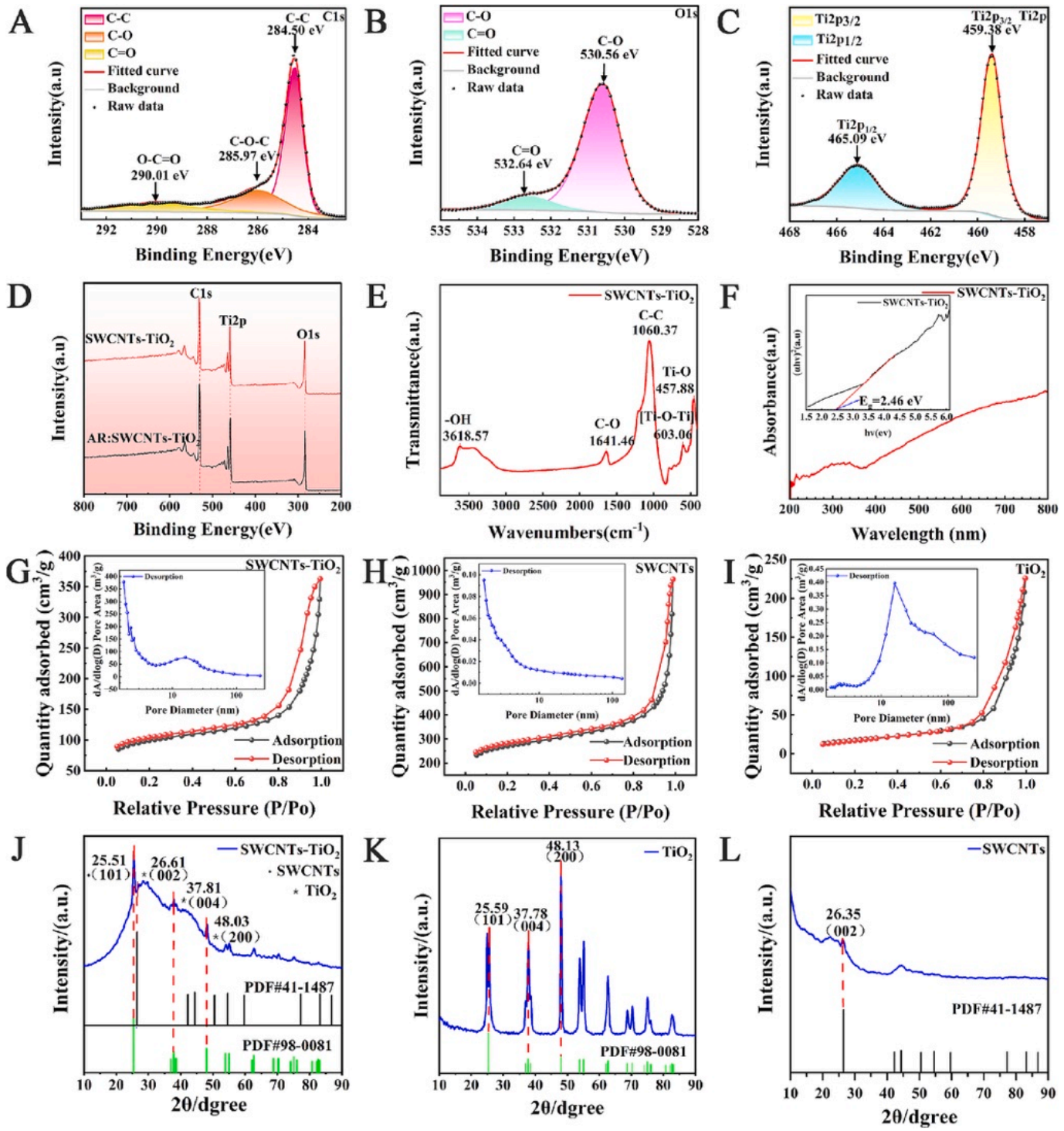

Fig. 3. Performance characterization of SWCNTs-TiO_2 Nanomaterials. (A)Peak spectra of C element in SWCNTs-TiO_2; (B)Peak spectra of O element in SWCNTs-TiO_2; (C)Peak spectra of Ti element in SWCNTs-TiO_2; (D)Total spectra of SWCNTs-TiO_2; (E)IR spectrum of SWCNTs-TiO_2; (F)UV spectrum of SWCNTs-TiO_2; (G)Nitrogen adsorption-desorption profiles of SWCNTs-TiO_2; (H)Nitrogen adsorption-desorption profiles of SWCNTs; (I)Nitrogen adsorption-desorption profiles of TiO_2. (J)XRD spectrum of SWCNTs-TiO_2; (K)XRD spectrum of TiO_2; (L)XRD spectrum of SWCNTs.

peaks of C1s, Ti2p, and O1s distinguishable in the XPS spectrum.

The Fourier Transform Infrared Spectroscopy (FT-IR) spectrum of SWCNTs-TiO_2 is analyzed in Fig. 3E. Characteristic peaks at 1641.46 cm^{-1} (C—O stretching vibration), 1060.37 cm^{-1} (C—C vibration), 603.06 cm^{-1} ([Ti-O-Ti] ring vibration), and 457.88 cm^{-1} (Ti—O vibration) strongly indicate the successful loading of TiO_2 onto SWCNTs [36,41]. The Ti-O-C bonds formed at the interface between SWCNTs and TiO_2 can effectively inhibit charge recombination, significantly improve the efficiency of interface electron transfer, provide an efficient charge transfer channel for electrocatalytic reactions, and thus contribute to excellent electrocatalytic performance.

The electrocatalytic activity of the SWCNTs-TiO_2 material in the Ultraviolet (UV) region was characterized using Ultraviolet-Visible Spectroscopy (UV–Vis) spectroscopy. As presented in Fig. 3F, when irradiated with UV light, the SWCNTs-TiO_2 material exhibited remarkable absorption characteristics. The absorption intensity of the material

increased gradually as the wavelength decreased from 800 nm to 200 nm. By comparing with the existing research, the successful modification of the material was verified [35,42,43].

Thermogravimetric Analysis (TGA) using a thermogravimetric synchronous analyzer was carried out to evaluate the thermal stability of the materials. The samples were heated from 20 to 800 °C at a heating rate of 25 °C· min^{1}. Additionally, nitrogen adsorption/desorption measurements were performed on SWCNTs-TiO_2, SWCNTs, and TiO_2, and the results are presented in Fig. 3G, H, and I. In the range of P/P_o approximately 0.8–1, steep capillary condensation and evaporation processes were observed. The narrow hysteresis loops and large adsorption range of SWCNTs-TiO_2 indicated a homogeneous and well-defined pore structure. The differences in average pore diameters result in variations of SWCNTs-TiO_2, SWCNTs, and TiO_2, leading to variations in the specific surface area, as summarized in Table 2 [44–47].

X-ray Diffraction (XRD) was further used to investigate the crystal structure of the nanomaterials. The XRD pattern of SWCNTs-TiO_2 showed four characteristic diffraction peaks at 25.51°(101) , 26.61°(002) , 37.81°(004), and 48.03°(200) in Fig. 3J. These diffraction peaks matched well with the reported structures of SWCNTs and TiO_2, confirming the successful synthesis of the composite with high crystallinity. Meanwhile, XRD tests were also performed on pure TiO_2 (Fig. 3K) and pure SWCNTs (Fig. 3L). As shown in Fig. 3K, the XRD pattern of pure TiO_2 exhibited three characteristic peaks at 25.59°, 37.78°, and 48.13°, corresponding to the (101), (004), and (200) lattice planes, respectively. As shown in Fig. 3L, the XRD pattern of pure SWCNTs showed one characteristic peak at 26.35°, which was assigned to the (002) lattice plane. All the lattice planes observed in the individual materials were present in the composite, which further confirmed the effective synthesis of the SWCNTs-TiO_2 nanocomposite. In addition, the peaks that appeared exclusively in the composite may be attributed to new crystal plane information generated by the successful composite modification of the materials [37,40,48–50].

3.3. The electrochemical properties of the dual-enzyme SWCNTs-TiO_2/SPCE sensor

Firstly, the SWCNTs-TiO_2/SPCE electrode was subjected to anodic oxidation in a 0.2 mol/L phosphate-buffered saline (PBS) solution with a pH of 6.0. This was carried out at an applied potential of +1.8 V for 300 s. Subsequently, Cyclic Voltammetry (CV) was performed within a potential range of −0.8 V to +1.0 V at a scan rate of 100 mV/s. This process was repeated until a stable cyclic voltammogram was obtained, resulting in the electrochemically pre-treated SWCNTs-TiO_2/SPCE electrode.

The constructed nanomaterial-modified dual-enzyme biosensor was placed in the aspartame standard solution to be tested, and CV tests were conducted during the reaction to verify the occurrence of redox reactions. As shown in Fig. 4A, the CV curve of the SWCNTs-TiO_2 composite-modified electrode exhibited symmetric redox peaks, confirming the occurrence of redox reactions. Aspartame molecules were decomposed by the dual-enzyme system on the electrode surface to generate Hydrogen Peroxide (H_2O_2), which underwent redox reactions to produce active hydroxyl ions, causing fluctuations in the CV curve. The appearance of the reduction peak directly indicated good reversibility of the electrochemical reaction and efficient electron transfer on the electrode surface. The SWCNTs-TiO_2 composite showed distinct current response characteristics at different potentials: the current gradually increased with increasing potential, with relatively low current response in the negative potential region and significantly enhanced response in the positive potential region, demonstrating improved electrochemical activity under positive potentials.

Table 2
Textural properties of SWCNTs-TiO_2, TiO_2 and SWCNTs.

Thermal properties	SWCNTs-TiO_2	TiO_2	SWCNTs
Specific surface area (m^2/g)	319.618	63.6104	869.674
Pore volume (cm^3/g)	0.561546	0.349555	1.48931
Average pore diameter (nm)	7.02772	21.9810	14.6517

LSV was used to characterize the electrochemical properties of SWCNTs-TiO_2/SPCE, with comparisons made to the LSV curves of bare SPCE, TiO_2/SPCE, and SWCNTs/SPCE. As shown in Fig. 4B, the current density of SWCNTs-TiO_2/SPCE increased significantly as the scan potential transitioned from negative to positive, and maintained a steady growth in the positive potential range—indicating high electrochemical activity and good stability of the composite within this potential range. Compared with TiO_2/SPCE, SWCNTs/SPCE, and bare SPCE, the LSV curve of SWCNTs-TiO_2/SPCE showed a wider current density variation range, significantly higher overall current level, and more obvious current growth trend with potential. Additionally, the onset oxidation potential of the target (Aspartame) was notably negatively shifted compared to that of single-component TiO_2/SPCE, reflecting the composite's ability to effectively reduce the activation energy of the target's oxidation reaction. From the mechanism perspective, Hydroxyl groups (-OH) on the TiO_2 surface can specifically adsorb target molecules, providing sufficient active sites for electrocatalytic reactions. Meanwhile, the highly conductive network constructed by SWCNTs accelerates electron transfer of the adsorbed molecules. The synergistic effect of these two components significantly enhances the electrocatalytic efficiency of the electrode [34,37,51].

In this study, Electrochemical Impedance Spectroscopy (EIS) tests were performed at open-circuit potential (OCP) by applying voltage within a specific frequency range, and the results were compared with the Linear Sweep Voltammetry (LSV) curves of bare SPCE, TiO_2/SPCE, and SWCNTs/SPCE. As shown in Fig. 4C, the EIS plot of SWCNTs-TiO_2/SPCE exhibited a typical semicircular shape, with a significantly smaller semicircle diameter than that of single-component TiO_2/SPCE, single-component SWCNTs/SPCE, and bare SPCE. This indicated a notable reduction in the charge transfer resistance (Rct) of the composite-modified electrode. A smaller Rct value implies lower electron transfer resistance at the electrode-electrolyte interface, faster electron transfer rate, and superior electron transfer capability, which also confirms the enhanced electrical conductivity of the composite [35,41,42].

The same set of tests was conducted on SWCNTs-TiO_2/SPCE after 10 cycles of aspartame solution detection, with results shown in Fig. 4D, E, and F. In Fig. 4A, the CV curve of the SWCNTs-TiO_2 composite exhibited a wide current density range and strong response. In contrast, Fig. 4D (CV curve after 10 measurements) showed significantly reduced current density, drastically narrowed current variation range, obvious curve fluctuations, and unstable current changes. This indicates that after multiple measurements, the electrochemically active sites on the electrode surface may be lost due to impurity adsorption or slight material detachment, leading to decreased electron transfer efficiency and electrochemical reaction activity. However, the electrode still maintained a certain level of electrochemical response, reflecting the sensor's moderate stability. In Fig. 4B, the LSV curve of SWCNTs-TiO_2/SPCE showed a wide current density variation range and a significant growth trend. In Fig. 4E (LSV curve after 10 measurements), the current density was drastically reduced, and the growth rate with potential slowed down significantly. This suggests that the electrocatalytic ability of the electrode attenuated after multiple measurements, possibly due to the compromised integrity of the composite modification layer on the electrode surface, which weakened its catalytic effect on electrochemical reactions. Comparison between Fig. 4F (EIS after 10 measurements) and Fig. 4C: The EIS plot of SWCNTs-TiO_2/SPCE in Fig. 4C showed a small semicircle diameter and low Rct. In contrast, Fig. 4F exhibited a significantly larger semicircle diameter (and higher overall impedance range), indicating a marked increase in Rct and reduced electron transfer rate at the electrode interface. This may be attributed to the formation of a thin adsorption layer on the electrode surface, which increased charge transfer resistance. This change is consistent

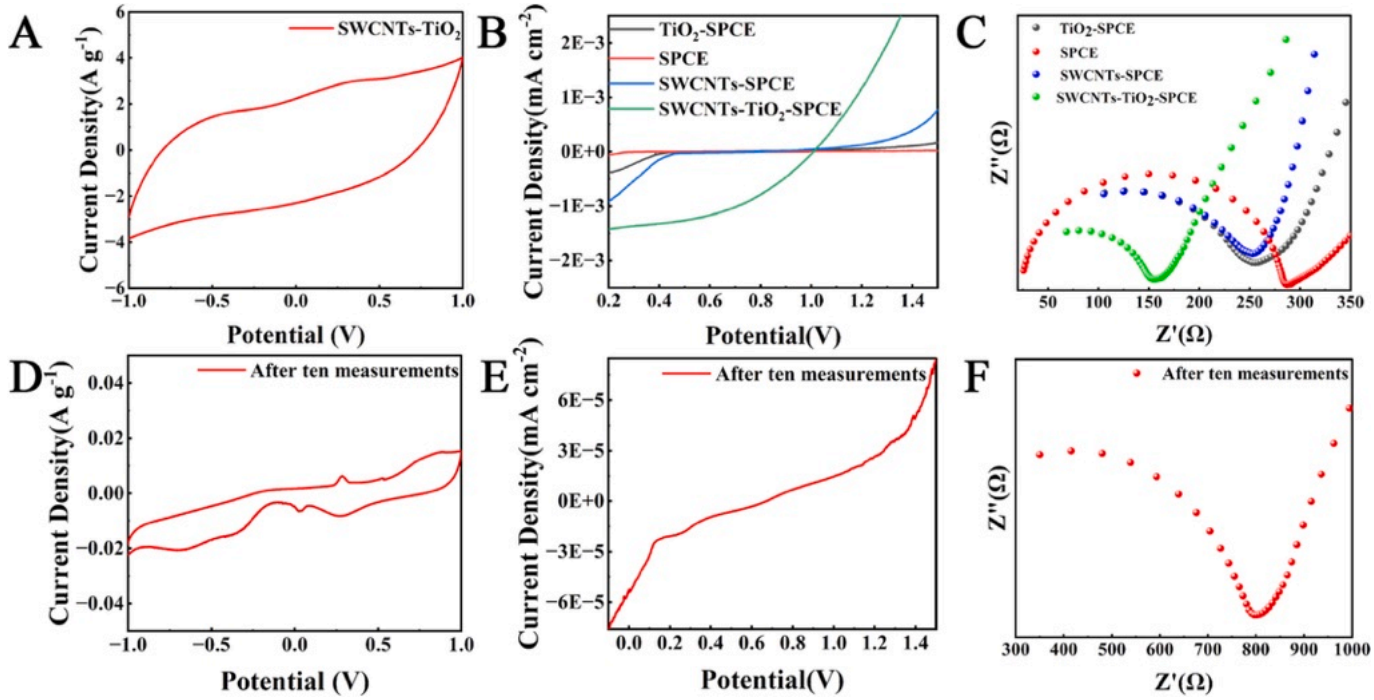

Fig. 4. Electrochemical properties of SWCNTs-TiO_2/SPCE dual-enzyme sensor. (A)SWCNTs-TiO_2/SPCE CV curve; (B)SWCNTs-TiO_2/SPCE LSV curve; (C)SWCNTs-TiO_2/SPCE EIS curve; (D)SWCNTs-TiO_2/SPCE (After ten measurements) CV curve; (E)SWCNTs-TiO_2/SPCE LSV (After ten measurements) curve; (F)SWCNTs-TiO_2/SPCE (After ten measurements) EIS curve.

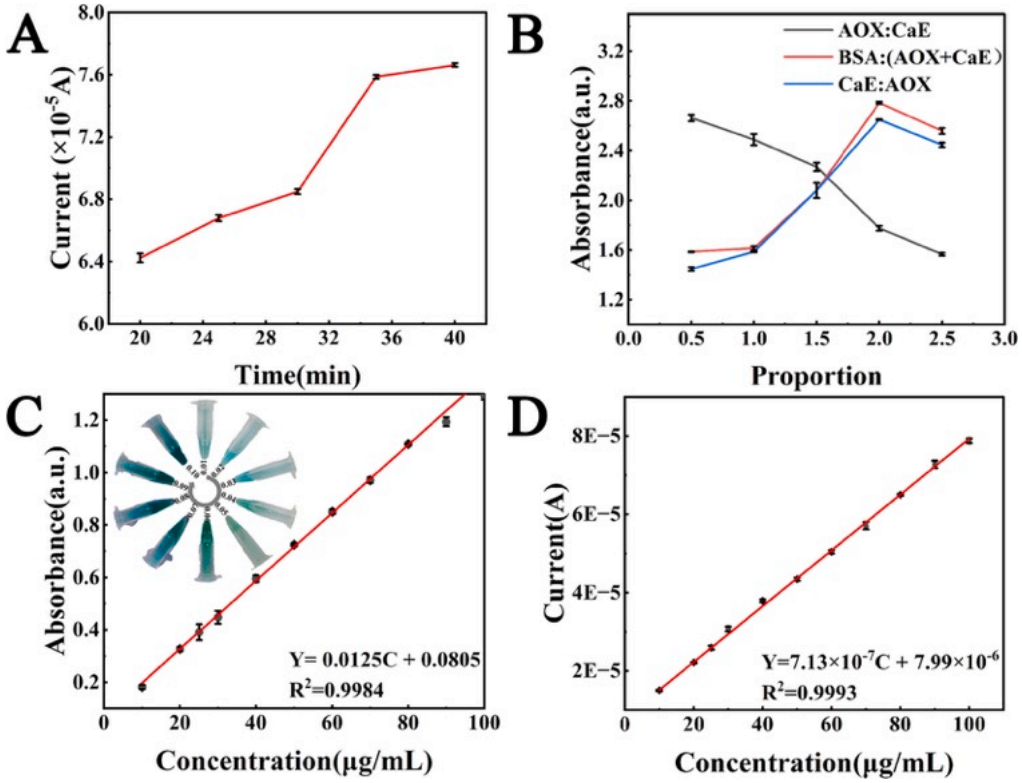

Fig. 5. Optimization of ultrasonication time and enzyme proportions and the standard curve of aspartame and the colorimetric degree classification image(Error bars represent the standard deviation of 3 parallel experiments). (A)Current response vs ultrasonic time; (B)Absorbance under different AOX, CaE, and BSA proportion combinations; (C)The standard curve of aspartame concentration ranging from 0.01 to 0.1 mg/mL(Tested by colorimetric methods) and the changing color of aspartame concentration ranging from 0.01 to 0.1 mg/mL;(D)The standard curve of aspartame concentration ranging from 0.01 to 0.1 mg/mL(Tested by electrochemical methods).

with the results of the previous two electrochemical characterizations, which all demonstrate decreased electrochemical performance of the electrode after multiple uses. From a practical application perspective, the sensor still enabled effective electrochemical detection after 10 cycles, which indirectly reflects the moderate stability and practicality of the SWCNTs-TiO_2 composite-modified electrode [51–53].

3.4. Optimization of synthetic and detection conditions

Ultrasonication time affected SWCNTs-TiO_2 dispersion. As shown in Fig. 5A, under the condition that all other factors are the same, the ultrasonic time of the composite material was controlled at 20, 25, 30, 35, and 40 min, and five sensors were prepared. The electrochemical response signal of the material increased significantly at 35 min of ultrasonic treatment, with only a marginal further increase at 40 min. Considering time efficiency, 35 min was chosen as the optimal ultrasonic duration.

The ratio of Aldehyde Oxidase (AOX), Carboxylesterase (CaE), and Bovine Serum Albumin (BSA) also affects the detection performance of the sensor. To explore the optimal ratio, we conducted experimental verification under the condition where the ratios of AOX: CaE, CaE: AOX, and BSA:(CaE + AOX) were set to 0.5:1.0, 1.0:1.0, 1.5:1.0, 2.0:1.0 and 2.5:1.0, respectively. During the experiment, when the ratio of one pair of enzymes (or BSA to the enzyme mixture) was adjusted, the ratios of the other components were maintained at their previously optimized values to eliminate interference from other variables. As illustrated in Fig. 5B, the sensor exhibited the best detection performance when the ratios of AOX: CaE, CaE: AOX, and BSA:(CaE + AOX) were 0.5:1.0, 2.0:1.0, and 2.0:1.0, respectively.

To evaluate the retention of enzyme activity over time, the biosensor was stored in the dark at 4 °C, and its response performance was measured periodically. The results showed that no significant decline in enzyme activity was observed within 7 days: when detecting aspartame standard solutions of the same concentration, the change rate of the response signal was ≤20 % compared with the freshly prepared biosensor, confirming that the enzyme activity could be effectively maintained during this period. All the above experimental results were verified by 3 parallel experiments, ensuring the reliability of the data. To verify the specificity of the sensor, we expanded the types of interfering substances to cover more than 5 common food additives, including sucralose, acesulfame-K, saccharin, sodium saccharin, and cyclamate. We used "interference rate" as a quantitative indicator to evaluate the degree of interference by comparing the difference in electrochemical response between "target analyte only" and "target analyte + interfering substances": the control group was a PBS solution containing only 0.5 mg/mL aspartame, and its oxidation peak current was measured. The interference group was a mixed solution containing 0.5 mg/mL aspartame +0.5 mg/mL of each of the 5 interfering substances, and its oxidation peak current was measured. The calculated interference rate was 3.2 %, and an interference rate < 5 % is considered no significant interference, which meets the requirements for food detection.

3.5. Testing of the actual samples

An external standard method was employed for quantification. A stock solution of aspartame (≥99 % purity). The concentrations of the standard solution were divided into 10 concentration gradients within the range of 0.01–0.1 mg/mL. All standard solutions were stored in a refrigerator at 4 °C and remained valid for 30 days. For the carbonated beverage samples, 5.000 g (accurate to 0.001 g) were weighed into a 50 mL beaker and degassed in a water bath at 50 °C to remove the carbon dioxide. The samples were then transferred quantitatively to a 25 mL volumetric flask and diluted to the required volume with deionized water.

As shown in Fig. 5C, Verification via the colorimetric method showed that within the same concentration range of 0.01–0.1 mg/mL, the linear regression equation between aspartame concentration (C, unit: μg/mL) and absorbance at 652 nm (A, unit: a.u.) was $A = 0.0125C + 0.0805$ with a linear correlation coefficient (R^2 of 0.9984), indicating an extremely strong concentration-absorbance correlation and excellent linear fitting degree. The LOD calculated by the "3 × standard deviation of blank signal/slope" formula was 0.232 μg/mL, which can fully cover the actual added concentration range of aspartame in food and meet the demand for low-concentration detection. As shown in Fig. 5C, for aspartame solutions with concentrations ranging from 0.01 to 0.1 mg/mL, distinct gradient color changes in the blue hue were observed. As shown in Fig. 5D, Verification Via Linear Sweep Voltammetry (LSV) showed that within the concentration range of 0.01–0.1 mg/mL, the linear regression equation between the sensor's oxidation peak current (I, unit: 1×10^{-5} A) and aspartame concentration (C, unit: μg/mL) was $I = 7.13 \times 10^{-7}C + 7.99 \times 10^{-6}$ with a linear correlation coefficient (R^2 of 0.9993), indicating an extremely strong concentration-current correlation and excellent linear fitting degree. The limit of detection (LOD) calculated by the formula "3 × standard deviation of blank signal/slope" was 0.131 μg/mL. Meanwhile, we have compared the above results with aspartame detection methods reported in recent literature, such as High-performance Liquid Chromatography (HPLC), Liquid Chromatography-tandem Mass Spectrometry (LC-MS/MS), and Ultraviolet-visible Spectrophotometry (UV-VIS): the LOD of this sensor is basically comparable to that of these large-scale high-precision instruments, with the electrochemical method reducing the LOD by approximately 50 %, shortening the detection time to 4–6 min, and significantly improving sensitivity and efficiency. Compared with HPLC, which requires a detection time of 25–35 min, this sensor has a faster detection speed and no need for complex pretreatment. It also has an advantage in cost, as the cost of fabricating one sensor is much lower than that of purchasing a large-scale instrument.

As shown in Table 3, the samples were divided into three concentration gradients. Colorimetric method and electrochemical detection method were employed for separate detection, and High-performance Liquid Chromatography (HPLC), a standard method, was used for verification. The detection results were satisfactory, with low Relative Standard Deviation (RSD). The content of aspartame in the actual samples measured in this study was basically consistent with that determined by the gold standard method. As shown in Table 4, spike recovery verification was performed for the two methods. Since the background value in the actual samples was non-negligible, precise spiking was adopted. The errors caused by experimental operations were within the allowable range, and the spike recoveries fell in the range of 91.8–110.57 %.

4. Conclusion

In conclusion, a dual-enzyme biosensor modified with a nanocomposite (SWCNTs-TiO_2) was designed, which can be used for rapid, sensitive, and visual detection of aspartame in food. The presence of the dual-enzyme system enables direct regulation of aspartame dissociation, and the generated Hydrogen Peroxide (H_2O_2) can react with 3,3′,5,5′-tetramethylbenzidine (TMB) in the electrolyte to produce a visible blue color. This performance benefit stems from the specific capture and decomposition of aspartame by the dual-enzyme system, as well as the electrochemical signal amplification effect of the nanocomposite. Therefore, the SWCNTs-TiO_2/SPCE (screen-printed carbon electrode) can be applied for rapid qualitative and quantitative detection of aspartame in food. Owing to the verification based on the different detection mechanisms of colorimetry and electrochemistry, this strategy allows mutual complementation and self-verification to ensure the reliability and accuracy of the results. Consequently, the constructed dual-enzyme biosensor modified with the SWCNTs-TiO_2 nanocomposite exhibits broad application prospects in the on-site monitoring of aspartame for food safety.

Table 3
Determination of aspartame in beverages by using Electrochemical, Colorimetric, and HPLC($n = 3$).

Samples	Concertration multiple	Electrochemical		Colorimetric		HPLC	
		Mean ± SD (μg/mL)	RSD (%)	Mean ± SD (μg/mL)	RSD (%)	Mean ± SD (μg/mL)	RSD (%)
1	0.7	8.14 ± 0.19	2.32	8.58 ± 0.38	4.45	7.39 ± 0.04	0.48
	1	12.09 ± 0.39	3.23	11.17 ± 0.17	1.53	10.74 ± 0.12	1.11
	1.3	15.78 ± 0.46	2.93	14.75 ± 0.46	3.12	13.68 ± 0.11	0.78
2	0.7	11.78 ± 0.17	1.47	9.56 ± 0.44	4.60	10.73 ± 0.19	1.80
	1	16.62 ± 0.19	4.33	13.21 ± 0.32	2.43	15.25 ± 0.3	1.95
	1.3	21.02 ± 0.37	1.77	17.22 ± 0.68	3.94	19.17 ± 0.57	2.97
3	0.7	8.27 ± 0.19	2.29	12.01 ± 0.43	3.60	8.76 ± 0.08	0.96
	1	12.54 ± 0.15	1.23	12.20 ± 0.27	2.18	12.53 ± 0.13	1.06
	1.3	15.31 ± 0.23	1.48	15.82 ± 0.52	3.27	16.69 ± 0.25	1.48
4	0.7	20.33 ± 0.75	3.69	20.02 ± 0.86	4.32	19.43 ± 0.45	2.31
	1	29.07 ± 0.93	3.18	24.62 ± 0.73	2.98	28.06 ± 0.43	1.52
	1.3	37.81 ± 0.83	2.19	33.87 ± 1.18	3.47	36.18 ± 0.58	1.62
5	0.7	11.82 ± 0.16	1.35	11.01 ± 0.47	4.30	9.76 ± 0.19	1.91
	1	16.25 ± 0.49	3.04	13.12 ± 0.21	1.60	13.70 ± 0.24	1.73
	1.3	20.71 ± 0.95	4.59	17.69 ± 0.36	2.02	18.19 ± 0.07	0.38

Table 4
Recorvey analysis of aspartame in the real samples with Electrochemical and Colorimetric methods(n = 3).

Samples	Electrochemical					Colorimetric				
	Added (μg/mL)	Total Concentration (μg/mL)	Total Founded (μg/mL)	Recovery (%)	RSD (%)	Added (μg/mL)	Total Concentration (μg/mL)	Total Founded (μg/mL)	Recovery (%)	RSD (%)
1	9.26	20.83	21.03 ± 0.37	102.16	1.77	9.56	21.51	21.60 ± 1.06	99.44	4.92
	11.57	23.14	22.94 ± 0.58	98.27	2.51	11.95	23.90	23.55 ± 0.99	97.11	4.22
	13.89	25.46	25.52 ± 0.73	100.45	2.84	14.34	26.29	26.90 ± 0.43	105.01	1.60
2	12.91	29.06	31.52 ± 0.08	119.10	0.26	11.03	24.82	25.76 ± 1.27	101.95	4.93
	16.14	32.29	32.85 ± 0.41	103.52	1.25	13.79	27.57	27.33 ± 0.97	98.22	3.56
	15.50	31.64	32.09 ± 0.08	102.91	0.25	16.55	30.34	31.60 ± 1.29	107.63	4.07
3	9.83	22.11	21.50 ± 0.51	93.57	2.37	10.31	23.20	22.17 ± 0.98	100.95	4.44
	12.29	24.57	24.01 ± 0.43	95.47	1.81	12.89	25.78	25.48 ± 0.74	97.69	2.90
	11.79	24.08	24.68 ± 0.61	105.10	0.94	15.47	28.36	27.50 ± 0.93	94.43	3.38
4	22.86	51.43	53.24 ± 0.50	107.93	2.49	20.81	46.82	45.13 ± 0.98	91.85	2.00
	28.57	57.14	58.05 ± 0.89	103.16	1.53	26.01	52.02	52.29 ± 1.96	101.02	3.75
	34.29	62.86	63.05 ± 0.30	100.56	0.47	31.21	57.22	56.13 ± 0.88	96.51	1.57
5	12.80	28.80	28.40 ± 0.17	96.88	0.61	10.93	24.59	24.87 ± 1.02	102.54	4.12
	16.00	32.00	31.21 ± 1.29	95.07	4.13	13.66	27.32	28.03 ± 0.72	105.20	2.56
	19.20	35.20	35.86 ± 0.27	103.44	0.76	16.39	30.05	31.78 ± 1.82	110.57	5.73

CRediT authorship contribution statement

Xin Li: Writing – original draft, Visualization, Validation, Methodology, Investigation, Formal analysis, Data curation, Conceptualization. **Lei Li:** Supervision, Software, Resources, Project administration, Funding acquisition, Formal analysis. **Ping Jiang:** Writing – review & editing, Supervision, Software, Resources, Project administration, Funding acquisition, Conceptualization.

Declaration of competing interest

The authors declare that they have no known competing financial interests or personal relationships that could have appeared to influence the work reported in this paper.

Acknowledgements

This work was supported by the Open Project of Changzhou Institute of Public Health, Nanjing Medical University (CPHN202304) and National College Students' Innovation and Entrepreneurship Training Program Project (202410312074Z).

Appendix A. Supplementary data

Supplementary data to this article can be found online at https://doi.org/10.1016/j.microc.2025.115528.

Data availability

Data will be made available on request.

References

[1] T. Zhang, T. Wang, K. Yu, C. Huang, K. Bao, Aspartame and ischemic stroke: unraveling the molecular link through network toxicology and molecular docking analysis, Sci. Rep. 15 (1) (2025) 23871–23884, https://doi.org/10.1038/s41598-025-08898-z.
[2] S.A. Singh, S. Singh, R.F. Begum, S. Vijayan, C. Vellapandian, Unveiling the profound influence of sucralose on metabolism and its role in shaping obesity trends, Frontiers in Nutrition 11 (2024) 1387646–1387659, https://doi.org/10.3389/fnut.2024.1387646.
[3] J.E. Goodman, D.N. Boon, M.M. Jack, Perspectives on recent reviews of aspartame cancer epidemiology, Global Epidemiology 6 (2023) 100117–100123, https://doi.org/10.1016/j.gloepi.2023.100117.
[4] T. Tangtawewipat, S. Thanachasai, Amperometric bienzymatic biosensor in flow injection analysis system for determination of aspartame in foods, Food Sci. Biotechnol. 33 (2) (2023) 343–354, https://doi.org/10.1007/s10068-023-01347-5.
[5] P. Kubica, J. Namieśnik, A. Wasik, Determination of eight artificial sweeteners and common Stevia rebaudiana glycosides in non-alcoholic and alcoholic beverages by reversed-phase liquid chromatography coupled with tandem mass spectrometry, Anal. Bioanal. Chem. 407 (5) (2014) 1505–1512, https://doi.org/10.1007/s00216-014-8355-x.
[6] S.A.A. Shaher, D.F. Mihailescu, B. Amuzescu, Aspartame safety as a food sweetener and related health hazards, Nutrients 15 (16) (2023) 3627–3654, https://doi.org/10.3390/nu15163627.
[7] B.T. Steffen, D.R. Jacobs, S.-Y. Yi, S.J. Lees, J.M. Shikany, J.G. Terry, C.E. Lewis, J. J. Carr, X. Zhou, L.M. Steffen, Long-term aspartame and saccharin intakes are related to greater volumes of visceral, intermuscular, and subcutaneous adipose

tissue: the CARDIA study, Int. J. Obes. (Lond) 47 (10) (2023) 939–947, https://doi.org/10.1038/s41366-023-01336-y.
[8] L.V. Griebsch, E.L. Theiss, D. Janitschke, V.K.J. Erhardt, T. Erhardt, E.C. Haas, K. N. Kuppler, J. Radermacher, O. Walzer, A.A. Lauer, et al., Aspartame and its metabolites cause oxidative stress and mitochondrial and lipid alterations in SH-SY5Y cells, Nutrients 15 (6) (2023) 1467–1488, https://doi.org/10.3390/nu15061467.
[9] Y.-C. Chen, Y.-C. Yeh, Y.-F. Lin, H.-K. Au, S.-M. Hsia, Y.-H. Chen, R.-H. Hsieh, Aspartame consumption, mitochondrial disorder-induced impaired ovarian function, and infertility risk, Int. J. Mol. Sci. 23 (21) (2022) 12740–12756, https://doi.org/10.3390/ijms232112740.
[10] K. Iizuka, Is the use of artificial sweeteners beneficial for patients with diabetes mellitus? The advantages and disadvantages of artificial sweeteners, Nutrients 14 (21) (2022) 4446–4456, https://doi.org/10.3390/nu14214446.
[11] D. Chen, X. Hou, Aspartame carcinogenic potential revealed through network toxicology and molecular docking insights, Sci. Rep. 14 (1) (2024) 11492–11501, https://doi.org/10.1038/s41598-024-62461-w.
[12] J. Somerson, K. Plaxco, Electrochemical aptamer-based sensors for rapid point-of-use monitoring of the mycotoxin ochratoxin a directly in a food stream, Molecules 23 (4) (2018) 912–918, https://doi.org/10.3390/molecules23040912.
[13] J.-W. Xu, Z.-M. Cui, Z.-Q. Liu, F. Xu, Y.-S. Chen, Y.-L. Luo, Organic–inorganic nanohybrid electrochemical sensors from multi-walled carbon nanotubes decorated with zinc oxide nanoparticles and in situ wrapped with poly(2-methacryloyloxyethyl ferrocenecarboxylate) for detection of the content of food additives, Nanomaterials 9 (10) (2019) 1388–1406, https://doi.org/10.3390/nano9101388.
[14] L. Geng, H. Dong, Q. Han, X. Huang, J. Huang, H. Wang, R. Xu, J. Zhao, Z. Wang, S. Wu, et al., Dual-recognition strategy sensor based on GO-SELEX aptamer screening for high-specificity identification of fenthion and its major metabolites in vegetables, Food Biosci. 69 (2025) 106969–106982, https://doi.org/10.1016/j.fbio.2025.106969.
[15] L. Geng, H. Wang, Z. Li, J. Huang, X. Sun, Y. Guo, F. Du, Research progress on molecularly imprinted polymers (MIPs)-based sensors for the detection of organophosphorus pesticides, Food Chem. 490 (2025) 145137–145152, https://doi.org/10.1016/j.foodchem.2025.145137.
[16] L. Geng, J. Huang, H. Dong, H. Wang, R. Xu, Z. Yu, I.A. Darwish, Y. Guo, X. Sun, GO-SELEX-enhanced dual-recognition sensor for highly specific detection of azamethiphos, J. Hazard. Mater. 492 (2025) 138252–138264, https://doi.org/10.1016/j.jhazmat.2025.138252.
[17] M. Serdar, Z. Knežević, Determination of artificial sweeteners in beverages and special nutritional products using high performance liquid chromatography, Arch. Ind. Hyg. Toxicol. 62 (2) (2011) 169–173, https://doi.org/10.2478/10004-1254-62-2011-2084.
[18] A. Zygler, A. Wasik, A. Kot-Wasik, J. Namieśnik, Determination of nine high-intensity sweeteners in various foods by high-performance liquid chromatography with mass spectrometric detection, Anal. Bioanal. Chem. 400 (7) (2011) 2159–2172, https://doi.org/10.1007/s00216-011-4937-z.
[19] M. Grembecka, P. Baran, A. Błażewicz, Z. Fijałek, P. Szefer, Simultaneous determination of aspartame, acesulfame-K, saccharin, citric acid and sodium benzoate in various food products using HPLC–CAD–UV/DAD, Eur. Food Res. Technol. 238 (3) (2013) 357–365, https://doi.org/10.1007/s00217-013-2111-x.
[20] G.G. Buyukgoz, A.G. Bozkurt, N.B. Akgul, U. Tamer, I.H. Boyaci, Spectroscopic detection of aspartame in soft drinks by surface-enhanced Raman spectroscopy, Eur. Food Res. Technol. 240 (3) (2014) 567–575, https://doi.org/10.1007/s00217-014-2357-y.
[21] M.K. Gupta, A. Ghuge, M. Parab, Y. Al-Refaei, A. Khandare, N. Dand, N. Waghmare, A comparative review on high-performance liquid chromatography (HPLC), ultra performance liquid chromatography (UPLC) & high-performance thin layer chromatography (HPTLC) with current updates, Current Issues in Pharmacy and Medical Sciences 35 (4) (2022) 224–228, https://doi.org/10.2478/cipms-2022-0039.
[22] L. Tan, Q.-Y. Li, Y.-J. Li, R.-R. Ma, J.-Y. He, Z.-F. Jiang, L.-L. Yang, C.-Z. Wang, L. Luo, Q.-H. Zhang, C.-S. Yuan, Specific adsorption and determination of aspartame in soft drinks with a zein magnetic molecularly imprinted modified MGCE sensor, RSC Adv. 11 (22) (2021) 13486–13496, https://doi.org/10.1039/d0ra10824c.
[23] X. Zhao, X. Lai, B. Yan, P. Cao, Y. Peng, R. Zhang, X. Chen, D. Chen, H. Pei, Y. Wang, et al., A novel photoelectrochemical biosensor for sensitive detection of nucleic acids based on recombinase polymerase amplification and 3D-array titania nanorods, Int. J. Biol. Macromol. 296 (2025) 139528–139534, https://doi.org/10.1016/j.ijbiomac.2025.139528.
[24] X. Zhao, Y. Ou, R. Bai, J. Yin, G. Wang, J. Wang, X. Zhao, Y. Liang, Q. Li, In situ cleavage-based sortase A-mediated site-specific immobilization of beta2-adrenoceptor on gold surface for surface plasmon resonance measurement, Biosens. Bioelectron. 281 (2025) 117452–117462, https://doi.org/10.1016/j.bios.2025.117452.
[25] C.L.C. Carvalho, S.Q. Nascimento, T. Bertaglia, L.C.I. Faria, E.R. Manuli, G. M. Pereira, W.C. da Silva, C.M. Costa, J.F. Maestu, S. Lanceros-Méndez, et al., Sustainable electrochemical-magnetic biosensor fabricated from recycled materials for label-free detection of SARS-CoV-2 in human saliva, ACS Sensors 10 (3) (2025) 1970–1985, https://doi.org/10.1021/acssensors.4c03175.
[26] Z. Safaei Moghaddam, M. Kaykhaii, M. Khajeh, A.R. Oveisi, PCN-222 metal–organic framework: a selective and highly efficient sorbent for the extraction of aspartame from gum, juice, and diet soft drink before its spectrophotometric determination, BMC Chemistry 14 (1) (2020) 19–27, https://doi.org/10.1186/s13065-020-00674-6.
[27] E. Cantù, S. Tonello, G. Abate, D. Uberti, E. Sardini, M. Serpelloni, Aerosol jet printed 3D electrochemical sensors for protein detection, Sensors 18 (11) (2018) 3719–3732, https://doi.org/10.3390/s18113719.
[28] W. Cimmino, S. Esposito, P.M. Kalligosfyri, N. Iaccarino, S. Cinti, Chemometrics-assisted enhancement of electrochemical biosensor performance toward miRNA detection, Anal. Chem. 97 (15) (2025) 8182–8188, https://doi.org/10.1021/acs.analchem.4c05402.
[29] Y.-Y. Hou, J. Xu, F.-T. Wang, Z. Dong, X. Tan, K.-J. Huang, J.-Q. Li, C.-Y. Zuo, S.-Q. Zhang, Construction of an integrated device of a self-powered biosensor and matching capacitor based on graphdiyne and multiple signal amplification: ultrasensitive method for microRNA detection, Anal. Chem. 93 (46) (2021) 15225–15230, https://doi.org/10.1021/acs.analchem.1c03521.
[30] J. Xu, Y. Liu, K.-J. Huang, Y.-Y. Hou, X. Sun, J. Li, Real-time biosensor platform based on novel sandwich graphdiyne for ultrasensitive detection of tumor marker, Anal. Chem. 94 (49) (2022) 16980–16986, https://doi.org/10.1021/acs.analchem.2c04278.
[31] D. Tang, J. Shi, Y. Wu, H. Luo, J. Yan, K.-J. Huang, X. Tan, Flexible self-powered sensing system based on novel DNA circuit strategy and graphdiyne for thalassemia gene by rapid naked-eye tracking and open-circuit voltage, Anal. Chem. 95 (44) (2023) 16374–16382, https://doi.org/10.1021/acs.analchem.3c03841.
[32] J. Shi, S. Liu, P. Li, Y. Lin, H. Luo, Y. Wu, J. Yan, K.-J. Huang, X. Tan, Self-powered dual-mode sensing strategy based on graphdiyne and DNA nanoring for sensitive detection of tumor biomarker, Biosens. Bioelectron. 237 (2023) 115557–115565, https://doi.org/10.1016/j.bios.2023.115557.
[33] J. Shi, P. Li, Y. Huang, Y. Wu, J. Wu, K.-J. Huang, X. Tan, Y. Ya, Smartphone-assisted self-powered dual-mode biosensor designed on binary 3D DNA walkers mediated CRISPR/Cas12a system, Chem. Eng. J. 483 (2024) 14931–14940, https://doi.org/10.1016/j.cej.2024.149231.
[34] S.D. Delekar, A.G. Dhodamani, K.V. More, T.D. Dongale, R.K. Kamat, S.F. A. Acquah, N.S. Dalal, D.K. Panda, Structural and optical properties of nanocrystalline TiO_2 with multiwalled carbon nanotubes and its photovoltaic studies using Ru(II) sensitizers, ACS Omega 3 (3) (2018) 2743–2756, https://doi.org/10.1021/acsomega.7b01316.
[35] S. Mishra, N. Chakinala, G. Sethia, A.G. Chakinala, P.K. Surolia, Enhanced photocatalytic performance of bi-doped TiO_2 under sunlight and UV light: mechanistic insights and comparative analysis, Photochem. Photobiol. Sci. 23 (8) (2024) 1495–1507, https://doi.org/10.1007/s43630-024-00609-3.
[36] A. León, P. Reuquen, C. Garín, R. Segura, P. Vargas, P. Zapata, P. Orihuela, FTIR and Raman characterization of TiO_2 nanoparticles coated with polyethylene glycol as carrier for 2-Methoxyestradiol, Appl. Sci. 7 (1) (2017) 49–57, https://doi.org/10.3390/app7010049.
[37] C. Zhan, Y. Li, P.R. Sharma, H. He, S.K. Sharma, R. Wang, B.S. Hsiao, A study of TiO_2 nanocrystal growth and environmental remediation capability of TiO_2/CNC nanocomposites, RSC Adv. 9 (69) (2019) 40565–40576, https://doi.org/10.1039/c9ra08861j.
[38] C. Ong, W.N. Lee, Y.S. Tan, P. Ohberg, Y. Hayashi, T. Nishikawa, Y. Yap, Optical bandgap tuning in SnO_2–MoS_2 nanocomposites: manipulating the mass of SnO_2 and MoS_2 using sonochemical solution mixing, J. Mater. Sci. Mater. Electron. 36 (1) (2024) 6–25, https://doi.org/10.1007/s10854-024-14061-7.
[39] M. Shaban, A.M. Ashraf, M.R. Abukhadra, TiO_2 nanoribbons/carbon nanotubes composite with enhanced photocatalytic activity; fabrication, characterization, and application, Sci. Rep. 8 (1) (2018) 781–797, https://doi.org/10.1038/s41598-018-19172-w.
[40] T.I.T. Okpalugo, P. Papakonstantinou, H. Murphy, J. McLaughlin, N.M.D. Brown, High resolution XPS characterization of chemical functionalised MWCNTs and SWCNTs, Carbon 43 (1) (2005) 153–161, https://doi.org/10.1016/j.carbon.2004.08.033.
[41] F.M. Pennisi, A.L. Pellegrino, N. Licciardello, C. Mezzalira, M. Sgarzi, A. Speghini, G. Malandrino, G. Cuniberti, Synthesis, characterization and photocatalytic properties of nanostructured lanthanide doped β-$NaYF_4$/TiO_2 composite films, Sci. Rep. 12 (1) (2022) 13748–13758, https://doi.org/10.1038/s41598-022-17256-2.
[42] J. Sun, S. Yu, Z. Cui, L. Hu, B. Sun, B. Chen, Synthesis, characterization, and photocatalytic antibacterial activities of porous Ce-doped TiO_2 microspheres using pine pollen as novel biotemplates, J. Mater. Sci. 57 (32) (2022) 15276–15297, https://doi.org/10.1007/s10853-022-07388-1.
[43] J. Al-Osaimi, N. Al-Hosiny, S. Abdallah, A. Badawi, Characterization of optical, thermal and electrical properties of SWCNTs/PMMA nanocomposite films, Iran. Polym. J. 23 (6) (2014) 437–443, https://doi.org/10.1007/s13726-014-0238-7.
[44] A. Shahverdi, G. Soucy, Thermogravimetric analysis of single-walled carbon nanotubes synthesized by induction thermal plasma, J. Therm. Anal. Calorim. 110 (3) (2011) 1079–1085, https://doi.org/10.1007/s10973-011-2114-4.
[45] A. Deng, Y. Zhu, X. Guo, L. Zhou, Q. Jiang, Synthesis of various TiO_2 Micro-/Nano-structures and their photocatalytic performance, Materials 11 (6) (2018) 995–1005, https://doi.org/10.3390/ma11060995.
[46] S. Pethaperumal, G.T. Mohanraj, P.S. Kumar, Characterization of MWCNT and SWCNT functionalized by acid treatments and the effect of functionalized carbon nanotubes on electrical properties of PMMA-MWCNT and PMMA-SWCNT nanocomposites, Appl. Nanosci. 13 (6) (2023) 4167–4176, https://doi.org/10.1007/s13204-023-02838-x.
[47] M.V. Kharlamova, Advanced carbon nanostructures: synthesis, properties, and applications II, Nanomaterials 14 (24) (2024) 2026–2029, https://doi.org/10.3390/nano14242026.
[48] A.B. Younis, V. Milosavljevic, T. Fialova, K. Smerkova, H. Michalkova, P. Svec, P. Antal, P. Kopel, V. Adam, L. Zurek, K. Dolezelikova, Synthesis and characterization of TiO_2 nanoparticles combined with geraniol and their

synergistic antibacterial activity, BMC Microbiol. 23 (1) (2023) 207–216, https://doi.org/10.1186/s12866-023-02955-1.

[49] D. Kumar, K. Singh, V. Verma, H.S. Bhatti, Investigation of optical properties of pristine and functionalized single-walled carbon nanotubes, J. Mater. Sci. Mater. Electron. 26 (4) (2015) 2117–2126, https://doi.org/10.1007/s10854-014-2656-x.

[50] J.T. Eman, N.M. Muhammed, H.A. Firas, M.A. Aseel, M.J. Zena, M.R. Israa, M. Samira, T.A. Kalid, A. Kalida, A.I. Ahmed, et al., X-ray diffraction analysis for main peaks and the noises of single and multi-walled carbon nanotubes, Open Access Research Journal of Engineering and Technology 4 (2) (2023) 001–007, https://doi.org/10.53022/oarjet.2023.4.2.0055.

[51] A. Mir, M.A. Shah, Cyclic voltammetry response of TiO_2 nanostructures prepared via fast and facile microwave irradiation, Bull. Mater. Sci. 45 (3) (2022) 119–126, https://doi.org/10.1007/s12034-022-02703-7.

[52] A.T. Dimitrov, A. Tomova, A. Grozdanov, O. Popovski, P. Paunović, Electrochemical production, characterization, and application of MWCNTs, J. Solid State Electrochem. 17 (2) (2012) 399–407, https://doi.org/10.1007/s10008-012-1896-z.

[53] A.V. Ambika, N. Navya, S.R. Kiran Kumar, B.L. Suresha, Electrochemical determination of paracetamol by SWCNT-modified carbon paste electrode: a cyclic voltammetric study, Carbon Lett. 32 (5) (2022) 1287–1295, https://doi.org/10.1007/s42823-022-00354-6.